Material structure of two-/three-dimensional Si–C layers fabricated by hot-C^+-ion implantation into Si-on-insulator substrate

2017 Jpn. J. Appl. Phys. 56 04CB03

(http://iopscience.iop.org/1347-4065/56/4S/04CB03)

Japanese Journal of Applied Physics **56**, 04CB03 (2017) **REGULAR PAPER**
https://doi.org/10.7567/JJAP.56.04CB03

Material structure of two-/three-dimensional Si–C layers fabricated by hot-C^+-ion implantation into Si-on-insulator substrate

Tomohisa Mizuno[1*], Yuhsuke Omata[1], Yoshiki Nagamine[1], Takashi Aoki[1], and Toshiyuki Sameshima[2]

[1]*Department of Science, Kanagawa University, Hiratsuka, Kanagawa 259-1293, Japan*
[2]*Department of Engineering, Tokyo University of Agriculture and Technology, Koganei, Tokyo 184-8588, Japan*

*E-mail: mizuno@info.kanagawa-u.ac.jp

Received October 4, 2016; revised December 17, 2016; accepted January 11, 2017; published online March 8, 2017

We experimentally studied the material structures of two-/three-dimensional (2D/3D) silicon carbon layers $Si_{1-Y}C_Y$ with $Y \leq 0.25$ and $5 \leq N_L \leq 162$ [N_L is the atomic layer number of $Si_{1-Y}C_Y$)] on buried oxide (BOX), which were fabricated by hot-C^+-ion implantation into a (100) silicon-on-insulator (SOI) substrate before an oxidation process. A 2D Si layer was also fabricated as a reference. The C 1s spectrum obtained by X-ray photoemission spectroscopy shows that the implanted C atoms segregate at the oxide interface. Using a scanning transmission electron microscope and a high-resolution scanning transmission electron microscope to observe cross sections of $Si_{0.75}C_{0.25}$ layers, 2-nm-thick 3C-SiC layers were found be partially formed in the C segregation layer near the BOX interface. At $Y > 0.1$ and $5 \leq N_L \leq 162$, we observed very strong photoluminescence (PL) emission in the UV/visible regions from a 3C-SiC area and a $Si_{1-Y}C_Y$ area in the C segregation layer, whereas a 2D Si emitted weak PL photons only at $N_L < 10$. Thus, the silicon carbon technique is very promising for Si photonics and bandgap engineering in CMOS.

1. Introduction

Two-dimensional (2D) Si layers are key structures for realizing future CMOS devices, such as extremely thin silicon-on-insulator (ETSOI) and FinFET CMOS,[1,2] as well as Si photonic devices.[3–5] We experimentally demonstrated strong quantum confinement effects (QCEs) in 2D-Si,[6–11] such as phonon confinement effects (PCEs)[12–16] and the QCEs of 2D electrons.[17–19] In addition, since the photoluminescence (PL) emission from 2D-Si can be detected only when the number of Si atom layers N_L is less than 10, QCEs can modulate the energy-band structures of 2D-Si[20–22] when $N_L < 10$ and thus modulate Si crystals into a direct-bandgap material from indirect-bandgap 3D-Si.[4,16,20,23] We experimentally confirmed that the PL peak photon energy E_{PH} of the (100) 2D-Si layer[11] under a fully relaxed condition[11,24–26] agrees well with the theoretical E_G determined by the first-principles calculation of 2D-Si with the surface Si terminated by H atoms.[20]

The E_G of (100) 2D-Si can be controlled by the Si thickness d_S,[11,20] but is still lower than 1.9 eV.[11] As a result, the peak PL photon wavelength λ_{PL} is longer than 650 nm.[11] Therefore, to realize a high-speed source heterojunction transistor (SHOT) that can inject high-velocity carriers into a channel with low E_G from high-E_G source regions using a band offset kinetic energy,[27–29] it is required to develop a new technology for realizing a higher E_G in a local Si area without controlling d_S. In addition, the higher-E_G engineering is also suitable for visible/UV Si photonics. Actually, in 3D $Si_{1-Y}C_Y$, E_G increases with increasing Y,[30–32] and the PL intensity I_{PL} also increases with increasing Y.[30] Moreover, silicon carbide (SiC) nanostructures are also studied,[33] and there are many diverse polytypes in SiC structures whose physical properties depend on the polytype.[32,33] Therefore, 2D-$Si_{1-Y}C_Y$ is a candidate for local E_G and λ_{PL} engineering for future CMOS and Si photonic devices. We actually demonstrated very high E_{PH} (>2 eV) and strong PL emissions in the visible region (>400 nm) in a 2D-$Si_{1-Y}C_Y$ structure fabricated by hot-$^{12}C^+$-ion implantation into a (100) SOI substrate.[34] Moreover, we verified the strong Y dependence of E_{PH} and I_{PL}, and experimentally confirmed the Si–Si, Si–C, and C–C bonds in $Si_{0.86}C_{0.14}$ from the C 1s and Si 2p spectra obtained by X-ray photoemission spectroscopy (XPS).[34]

In this work, we experimentally studied material structures and band structure modulation of 2D-/3D-$Si_{1-Y}C_Y$ fabricated by hot-$^{12}C^+$-ion implantation into (100) SOIs at 900 °C, where $0.01 < Y \leq 0.25$, and $5 \leq N_L \leq 162$ ($0.5 \leq d_S \leq 20$ nm).[35] We observed the partial formation of 3C-SiC in the C segregation layers near the buried oxide (BOX) interface of $Si_{0.75}C_{0.25}$, using high-resolution transmission electron microscope (HRTEM) and high-angle annular-dark-field scanning TEM (HAADF-STEM). We verified very strong PL emission from $Si_{1-Y}C_Y$ at the BOX interface even at $N_L = 162$, and E_{PH} increases to 3 eV with Y increasing to 0.25. However, the E_{PH} of $Si_{1-Y}C_Y$ is independent of N_L, whereas the E_{PH} of 2D-Si rapidly increases with decreasing N_L, because of the QCEs of electrons in 2D Si. In this study, we show that the N_L dependence of PL properties in $Si_{1-Y}C_Y$ can be explained using the material structure model for $Si_{1-Y}C_Y$ layers.

2. Experimental procedure

High-quality and uniform $Si_{1-Y}C_Y$ layers were successfully fabricated by a simple process, namely, hot-$^{12}C^+$-ion implantation which suppresses the C-ion-induced damage in the Si layer before an oxidation process,[34] as shown in Fig. 1. Figure 1(b) shows the hot-C^+-ion implantation into a (100) 8-nm-thick SOI substrate at a substrate temperature of 900 °C, where the surface oxide thickness was 120 nm after thinning the Si layer by high-T (1000 °C) oxidation of an initially 55-nm-bonded SOI substrate[36] [Fig. 1(a)]. The C projection range was set to be in the middle of the Si layer. The d_S of $Si_{1-Y}C_Y$ layers was varied from 8 to 0.5 nm by changing the dry oxidation time (900 °C) as shown in Fig. 1(c), where d_S was evaluated by the UV–visible reflection method.[6] The d_S variation in 10^4 μm^2 area was estimated to be approximately 0.2 nm in this process.[7] As a result, $5 \leq N_L \leq 60$, where N_L ($\equiv d_S/d + 1$) which is a better indicator for evaluating the QCEs of 2D Si,[7] where d is the distance between two Si lattice planes and is 0.136 nm ($\equiv a_S/4$), and a_S is the lattice constant of Si in the case of (100) Si. The minimum N_L of 5 is almost the same as that of Si unit cell of 5. In addition, $Si_{1-Y}C_Y$ layers with a much larger N_L of 162 ($d_S = 22$ nm)

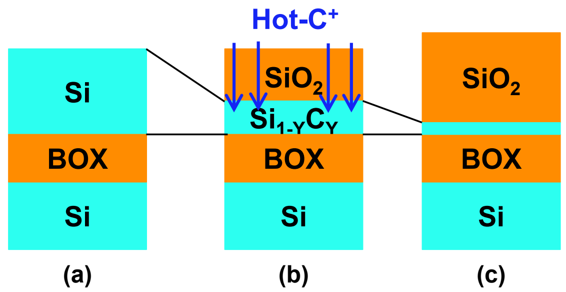

Fig. 1. (Color online) Schematic fabrication steps for $Si_{1-Y}C_Y$ layers. (b) Hot $^{12}C^+$ ion implantation into 8-nm-thick (100) SOI substrate at 900 °C was carried out after (a) 1000 °C dry oxidation of the initial 55-nm-thick SOI. D_C was varied from 5×10^{12} to 4×10^{16} cm^{-2} at $E_A = 32$ keV. (c) Additional 900 °C dry oxidation was carried out for thinning the thick $Si_{1-Y}C_Y$ layers, and d_S was controlled by adjusting oxidation time. In this study, $10^{-5} \le Y \le 0.25$, and the minimum N_L was 5.

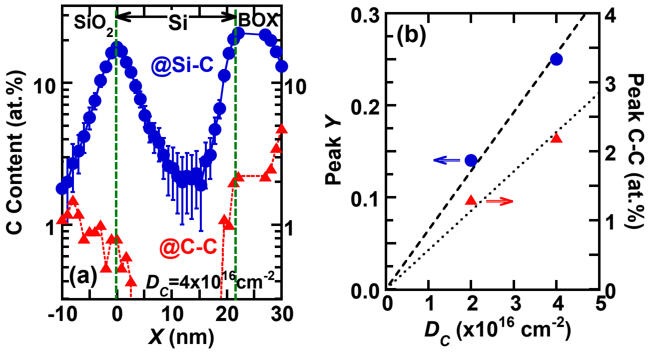

Fig. 2. (Color online) (a) Non-uniform depth profile of C atomic percent of Si–C and C–C (separated C) bonds in $Si_{1-Y}C_Y$ layers evaluated from the C 1s obtained by XPS just after hot-C$^+$-ion implantation process with $D_C = 4 \times 10^{16}$ cm^{-2}, where d_S is 22 nm. The detection limit of XPS is approximately 1 at. %. C atoms segregate at both the surface oxide and BOX interface, and the maximum Y at the BOX interface is 0.25, but the surface C segregation area disappears after the Fig. 1(c) step. Approximately 90% of C atoms bind to Si, but approximately 10% of C atoms precipitate at the BOX interface. (b) Peak-Y (left axis) at the BOX interface and peak C at. % (right axis) of C–C bond vs D_C, and both are proportional to D_C.

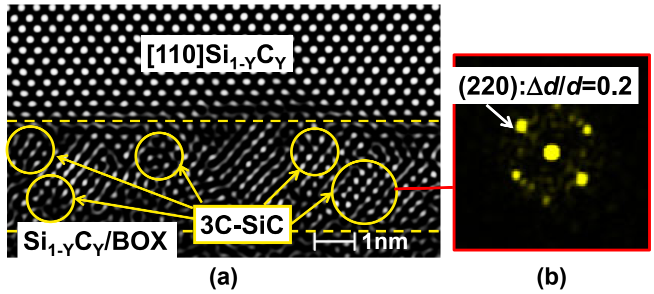

Fig. 3. (Color online) (a) HRTEM image of the cross section of 22-nm-thick $Si_{1-Y}C_Y$ layers at the [110] direction, where $D_C = 4 \times 10^{16}$ cm^{-2}. Near the BOX interface, approximately 2-nm-thick 3C-SiC layer was partially formed, shown in the circles. (b) The electron diffraction pattern of 3C-SiC obtained by FFT analysis of lattice spots in (a) shows a cubic, and d at (220) plane is approximately 0.25 nm in 3C-SiC, whereas the ED pattern of (220) at the center of the Si layer shows that d is approximately 0.31 nm. As a result, d of 3C-SiC is reduced by approximately 20%, compared with that of the Si layer, and the d reduction rate is equal to the lattice constant reduction of 3C-SiC compared with that of Si.

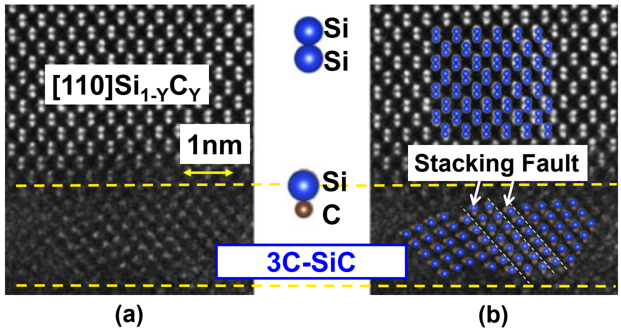

Fig. 4. (Color online) (a) HAADF-STEM image of the cross section of 22-nm-thick $Si_{1-Y}C_Y$ layers in the [110] direction, where $D_C = 4 \times 10^{16}$ cm^{-2}. (b) Schematic Si/Si and Si/C atom pairs are added in the Si and C segregation layers in Fig. 3(a), respectively. Si/Si and Si/C atom pairs are clearly observed in each layer, but some areas show unclear Si/C atom pairs. Here, the C atoms in the Si/C atom pair in the 3C-SiC layer are not clearly observed. The 3C-SiC thickness is approximately 2 nm. Moreover, some stacking faults are observed in 3C-SiC layers.

was also fabricated by hot-$^{12}C^+$-ion implantation into a (100) 22-nm-thick SOI substrate with a 87 nm surface oxide layer at a SOI substrate temperature of 900 °C without the step in Fig. 1(c), where the $^{12}C^+$ ion projection range was also set to be in the middle of the Si layer. Y was controlled by the $^{12}C^+$ ion dose D_C, where D_C was varied from 5×10^{12} to 4×10^{16} cm^{-2}. In this study, we analyzed the physical properties of the $Si_{1-Y}C_Y$ layer with a thick surface oxide, whose structure has silicon quantum wells (SQWs) composed of surface-oxide/$Si_{1-Y}C_Y$/BOX layers. A semiconductor layer with $N_L \le 10$ is defined by the 2D semiconductor, since Si with $N_L \le 10$ can emit PL photons obtained by the large band structure modulations.[7)]

On the basis of the C 1s spectra obtained by XPS, as shown in Fig. 2(a), we can obtain non-uniform depth profiles of C atomic percent of Si–C and C–C bonds in $Si_{1-Y}C_Y$ layers just after hot-C$^+$-ion implantation into 22 nm SOI, where $D_C = 4 \times 10^{16}$ cm^{-2}. Approximately 90% of C atoms bind to Si atoms, but approximately 10% of C atoms separate near the C segregation area at the BOX interface. It is noted that C atoms segregate at both of the oxide interfaces just after C$^+$ implantation, which is a characteristic feature of the hot-C$^+$-ion implantation process. The C segregation at the oxide interface is caused by the partial formation of 3C-SiC at the oxide interface, as shown in Figs. 3 and 4. On the other hand, we experimentally verified that the conventional C$^+$ ion implantation process at room temperature showed no segregation of C atoms at the oxide interface. Moreover, our previous work showed that this C atom segregation disappeared only at the surface oxide interface after the surface oxidation of Si layers, since C atoms near the surface oxide interface are chemically changed into CO gas and outgassed during the oxidation process.[34,37)] On the other hand, it was also found[34)] that the maximum Y at $Si_{1-Y}C_Y$/BOX interface remained nearly constant despite of the thinning of the Si layer, because the surface oxidation did not affect the BOX interface region. We also confirmed that the maximum Y attained just after hot-C$^+$-ion implantation into 8-nm-thick SOIs was 0.25. Thus, $Si_{1-Y}C_Y$ layers are mainly divided into the C segregation and very low C (<1 at. %) areas. Figure 2(b) shows the peak-Y and the separated C concentration (C–C bond) evaluated from the C 1s spectrum as a function of D_C, and both the peak Y and separated C concentration are proportional to D_C and independent of N_L (d_S).[34] Hereafter, the Y of $Si_{1-Y}C_Y$ layers is defined by the peak Y at the C segregation area at the BOX interface. Namely,

$$Y = 6.3 \times 10^{-18} D_C. \quad (1)$$

Moreover, Fig. 2(b) indicates that the C atom separation effects in the C segregation area monotonically increase with increasing D_C.

In this work, we experimentaly studied the material structures of $Si_{1-Y}C_Y$ layers by HRTEM, HAADF-STEM, and 325-nm-UV Raman spectroscopy. We analyzed novel band-structure modulations of 2D-/3D-$Si_{1-Y}C_Y$ layers and compared them with those of 2D Si by the PL method at room temperature. The excitation laser energy E_{EX} was varied from 2.3 to 3.8 eV. The excitation laser power P_L was set to be 1 mW to suppress the P_L heating effects on Si,[7] and the laser diameter was 1 µm. The PL spectrum in a wide range of photon wavelengths from the UV to NIR region was calibrated using a standard illuminant. The FWHM of the Si Raman LO peak was not degraded within 8% even at $D_C = 4 \times 10^{16}\,cm^{-2}$, which is the merit of the hot C^+ implantation technique. Thus, the hot C^+ ion implantation-induced damage in the Si layer is considered to be very small in this study.

3. Results and discussion

3.1 Material structures of 2D-/3D-$Si_{1-Y}C_Y$

First, we discuss the material structures of $Si_{1-Y}C_Y$, such as the Si/C atomic arrangement of $Si_{1-Y}C_Y$.

Figures 3(a) and 3(b) respectively show HRTEM images of the cross sections of 22-nm-thick $Si_{1-Y}C_Y$ layers in the [110] direction and the electron diffraction (ED) pattern of the C-segregation area near the BOX interface obtained by fast-Fourier-transform (FFT) analysis of lattice spots in Fig. 3(a), where $D_C = 4 \times 10^{16}\,cm^{-2}$. Figure 3(a) shows clear lattice spots at the center of $Si_{1-Y}C_Y$ layers even at the high C dose of $4 \times 10^{16}\,cm^{-2}$. However, the approximately 2-nm-thick C segregation area near the BOX interface indicates that the lattice spots are much different from those of the center of $Si_{1-Y}C_Y$ layers, and a clear enclosed in circles and an unclear lattice spots coexist. In addition, Fig. 3(b) shows that the clear lattice spots area enclosed in circles in Fig. 3(a) show a clear cubit ED pattern, and the spacing of the lattice plane d at the (220) plane is approximately 0.25 nm in 3C-SiC area, whereas the ED pattern of the (220) Si layer shows that d is approximately 0.31 nm. Thus, the spacing reduction rate of the (220) lattice plane $\Delta d/d$ compared with d of the Si layer is approximately 0.2, where $\Delta d/d \equiv (d - d_{3C})/d$ and d_{3C} is spacing between lattice plane in C-segregation area. The $\Delta d/d$ of other clear spots enclosed in circles is close to 0.2. This $\Delta d/d$ of the C-segregation area is the same as the lattice constant reduction rate $\Delta a/a_S$ [$\equiv (a_S - a_{3C})/a_S$] of 0.20 in bulk 3C-SiC, where a_{3C} and a_S are the lattice constants of bulk 3C-SiC ($\equiv 0.436$ nm) and Si ($\equiv 0.534$ nm), respectively.[33] Consequently, 3C-SiC layers in the 2-nm-thick C segregation area enclosed in circles in Fig. 3(a) are partially formed by hot-C^+-ion implantation, and thus the lower Y value of 0.25 shown in Fig. 2(a) can be explained by the partial formation of 3C-SiC, as shown in Fig. 4 in detail.

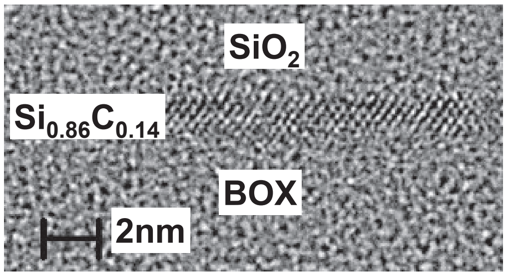

Fig. 5. HRTEM image of the cross section of 0.8-nm-thick $Si_{1-Y}C_Y$ layers, where $D_C = 2 \times 10^{16}\,cm^{-2}$. Uniform 2D $Si_{1-Y}C_Y$ layers with clear lattice spots can be successfully formed.

Next, Figs. 4(a) and 4(b) show the HAADF-STEM images of the cross sections of 22-nm-thick $Si_{1-Y}C_Y$ layers in the [110] direction near the BOX interface, and Fig. 4(a) additionally shows a schematic of a Si/Si and Si/C atom pairs, where $D_C = 4 \times 10^{16}\,cm^{-2}$. The center of $Si_{1-Y}C_Y$ layers shows clear Si/Si pairs, but the atomic pair in the C segregation area is markedly different from that in the center area of $Si_{1-Y}C_Y$ layers. Namely, most of the C segregation area shows a clear Si/C atom pair, whereas C atoms in the Si/C atom pair cannot be seen in this HAADF-STEM image. However, Fig. 4(b) shows that a portion of the C segregation area shows unclear Si/C atom pairs. Straight line spots of the Si/C atom pair without hexagonal structures also indicate the partial formation of approximately 2-nm-thick 3C-SiC layers in the C-segregation layers shown in Fig. 3(a) near the BOX interface. Thus, Figs. 3 and 4 show that 3C-SiC layers can be partially fabricated in the C-segregation area by this simple hot-C^+-ion implantation technique. The C content of 0.25 shown in Fig. 2(a) is too low to form full 3C-SiC layers, and thus, the C^+ ion dose should be increased to approximately $8 \times 10^{16}\,cm^{-2}$. On the other hand, Fig. 4(b) shows that some stacking faults are observed in 3C-SiC layers, and the stacking fault density is estimated to be approximately $2.5 \times 10^6\,cm^{-1}$, as shown by the visual field of Fig. 4(b). Thus, it is also required to optimize the fabrication process for Si–C layers to remove stacking faults by increasing the hot-ion implantation temperature.

Moreover, Fig. 5 also shows a HRTEM image of a cross section of a 0.8-nm-thick 2D $Si_{0.86}C_{0.14}$ layer, where $D_C = 2 \times 10^{16}\,cm^{-2}$. The HRTEM image shows uniform Si–C layers and clear lattice spots even in this 2D structure. Thus, even 2D $Si_{0.86}C_{0.14}$ layers can be successfully fabricated in this study.

3C-SiC layer formation can also be confirmed by UV-Raman spectroscopy. Figure 6(a) shows UV-Raman spectra of 2D Si (green line) and 2D $Si_{1-Y}C_Y$, where $E_{EX} = 3.8$ eV and $N_L = 5$. Red and blue lines are the data at $Y = 0.25$ and 0.14, respectively. The Raman peaks at 1600, 1400, and 960 cm^{-1} show the G and D bands of graphitic carbon[34,38] in 2D $Si_{1-Y}C_Y$, and the 2nd-order peak of 2D Si, respectively. Since the 2nd-order peak is enhanced by PCEs,[7] the weak LO mode (970 cm^{-1}) of Si–C vibration in 3C-SiC[38] cannot be observed in this study. Moreover, since it is reported that the 3C-SiC layer shows the G band of graphitic carbon,[32,33] the G band observation in Fig. 6(a) is a necessary condition for the successful formation of 3C-SiC near the BOX interface. The D band is probably attributable to C separation

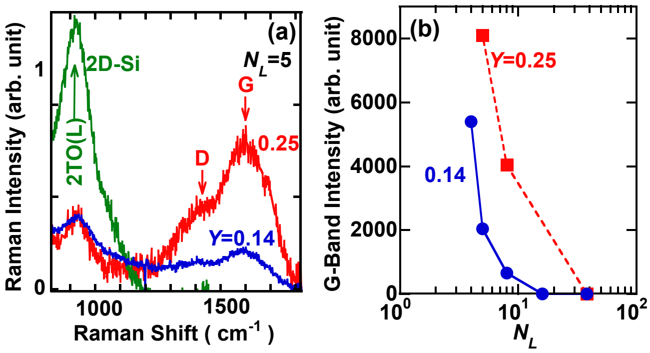

Fig. 6. (Color online) (a) Raman spectra of 2D Si (green line) and 2D $Si_{1-Y}C_Y$, where $E_{EX} = 3.8$ eV and $N_L = 5$. Red and blue lines show the data under $Y = 0.25$ and 0.14, respectively. The Raman peaks at 1600, 1400, and 960 cm^{-1} show the G and D bands of graphitic carbon in 2D $Si_{1-Y}C_Y$, and the 2nd-order peak of 2D Si, respectively. (b) Y dependence of G-band intensity of 2D $Si_{1-Y}C_Y$, where $E_{EX} = 3.8$ eV and $N_L = 5$. Red and blue lines show the data under Y of 0.25 and 0.14, respectively. The G-band intensity rapidly increases with increasing Y and decreasing N_L, and the successful observation of G band is the necessary condition to confirm 3C-SiC formation.

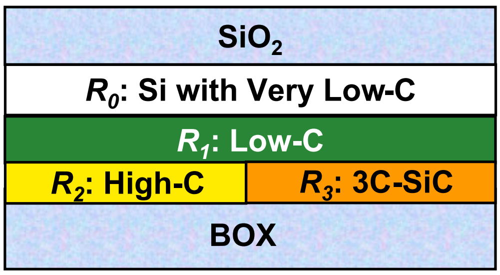

Fig. 7. (Color online) Schematic cross section of $Si_{1-Y}C_Y$ layers after the step in Fig. 1(c) under high-Y condition. C segregation layers are separated into three regions of the Si–C alloy at the C slope region (R_1), the Si–C layer (R_2) in the peak-C area, and the 3C-SiC layer (R_3) in the peak-C area near the BOX interface. The C segregation layers is expected to emit PL photons. On the other hand, the Si layer with $Y < 0.01$ (R_0) on the C segregation layers is thinned by the Fig. 1(c) step. Therefore, PL and Raman data of $Si_{1-Y}C_Y$ layers are considered to be superposed by the properties of the three regions from R_1 to R_3.

layers near the BOX interface. Figure 6(b) shows the Y dependence of the G-band intensity I_G of 2D $Si_{1-Y}C_Y$, and red and blue lines show the data at $Y = 0.25$ and 0.14, respectively, as the same data of Fig. 6(a). The G-band intensity rapidly increases with increasing Y and decreasing N_L, which leads to 3C-SiC formation only in the C segregation area under high-Y conditions.

Here, we summarize the material structures of thinned $Si_{1-Y}C_Y$ layers, as shown in Fig. 7. As shown in Figs. 3 and 4, in the high-C region of the C segregation layer, the partially formed 3C-SiC area (R_3) and the Si–C alloy area with high C concentration (R_2) coexist. The slope area of the low-C region of the C-segregation area and the thick Si layer with $Y \leq 0.01$ shown in Fig. 2(a) show the R_1 and R_0 areas, respectively. Since our previous study[34] showed that the thickness of the C segregation layer, that is, $R_1 + R_2$ or $R_1 + R_3$, remains almost constant despite of the thinning of the SOI [Fig. 1(c)], R_0 area can mainly thinned by increasing oxidation time. Since a thick R_0 area with $N_L > 8$ cannot emit PL photons,[6–11] it is expected that the three regions from R_1 to R_3 can emit their own PL photons; I_1, I_2, and I_3 with different E_{PH} values (E_1, E_2, and E_3), respectively. Depending on the Y value of the R_1, R_2, and R_3 areas, it is expected that $E_1 < E_2 < E_3$ and $I_1 < I_2 < I_3$, because our previous study[34] also showed that both E_{PH} and I_{PL} of $Si_{1-Y}C_Y$ layers increase with increasing Y.

Next, we discuss the material properties of R_0 area. The smaller lattice constants of the R_2 and R_3 areas at the BOX interface, compared with that of Si layer, are considered to induce a compressive strain in the R_0 area. We already showed the smaller lattice constant of the R_3 area of 3C-SiC ($\Delta a/a_S = 0.20$) in Fig. 3(b). On the other hand, assuming that the $Si_{1-Y}C_Y$ layer of the R_2 area consists of the Si and 3C-SiC alloys, the lattice constant of $Si_{1-Y}C_Y$ of the R_2 area, $a(Y)$, obeys Vegard's linear rule[32] for the a_S of bulk-Si and the a_{3C} of bulk 3C-SiC. Namely,

$$a(Y) = a_S - (a_S - a_{3C})\frac{Y}{0.5}. \tag{2}$$

Thus, using $a(Y)$ of Eq. (2), the $\Delta a/a_S$ of the R_2 area can be calculated using the following equation.

$$\frac{\Delta a(Y)}{a_S} = 2Y\frac{a_S - a_{3C}}{a_S} \approx 0.39Y. \tag{3}$$

When $Y = 0.25$, as shown in Fig. 2(a), the $\Delta a/a_S$ of the R_2 area is approximately 0.1. However, since the 3C-SiC (R_3) is partially formed, the C concentration of the R_2 area, close to the R_3 area, decreases, and thus the $\Delta a/a_S$ of the R_2 area is probably smaller than 0.1. As a result, the R_0 area on the R_2 region with a smaller $\Delta a/a_S$ and the R_0 area on the R_3 area with a larger $\Delta a/a_S$ are compressively strained, respectively. As a result, the latter strain is expected to be larger than the former strain. Thus, the compressive strain ε of the R_0 area fluctuates.

By fast-Fourier-transform-mapping (FFTM) analysis of lattice spots of HRTEM in Fig. 3(a), the biaxial compressive strain ε (%) is defined by $100(a_Y/a_X - 1)$, where a_Y and a_X are the lattice constants in the vertical and lateral directions in the HRTEM image shown in Fig. 3(a); thus the plus and minus signs of ε indicate the compressive and tensile strains, respectively. Figure 8(a) shows a contour map of biaxial ε, where $D_C = 4 \times 10^{16}$ cm^{-2} and $d_S = 22$ nm. The x- and y-axes in Fig. 8(a) show the lateral and vertical directions as in Fig. 2(a). Figure 8(a) clearly shows the compressive strain in the entire area, and the compressive strain is attributable to the small lattice constants of the R_2 and R_3 areas. As a result, ε fluctuates, as expected. A large ε area locally exists shown as blue regions of approximately 3 nm size, which is possibly due to the large $\Delta a/a_S$ of the R_3 area. Figure 8(b) also shows a histogram of biaxial ε prepared by the same data shown in Fig. 8(a). The ε distribution is of the Gaussian type, but clearly divides into two areas; the low-ε area with an average ε of 0.25% attributable to the small $\Delta a/a_S$ of the R_2 area and the high-ε area with the average ε of 1.7% attributable to the large $\Delta a/a_S$ of the R_3 area. Figure 8(b) shows that the frequency of R_2 is higher than that of R_3, which is attributable to the small area of R_3 shown as the blue area in Fig. 8(a). Thus, R_0 layers mainly consist of two regions; high- and low-compressive-strain regions. On the other hand, in the case of a low Y of 0.13 shown in Fig. 8(c), where $D_C = 2 \times 10^{16}$ cm^{-2} and $d_S = 4$ nm, the ε histogram shows only one Gaussian distribution with a lower average ε of 0.7%, which

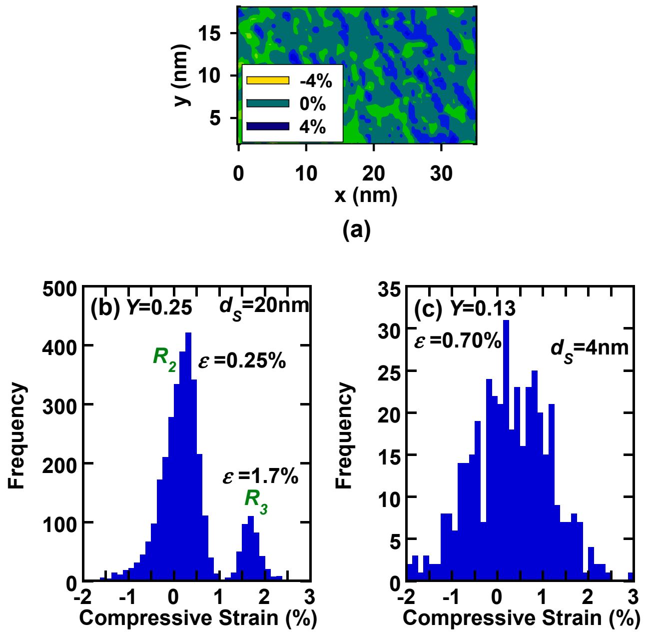

Fig. 8. (Color online) FFTM analysis of lattice spots of HRTEM image in Fig. 3(a). (a) Contour map of biaxial ε (plus shows a compressive strain) and (b) ε-histogram of Fig. 6(a) data under $d_S = 22\,\text{nm}$ and $D_C = 4 \times 10^{16}\,\text{cm}^{-2}$. (c) ε-histogram data under $d_S = 4\,\text{nm}$ and $D_C = 2 \times 10^{16}\,\text{cm}^{-2}$. X- and Y-axes in (a) respectively show the lateral and vertical directions in Fig. 3(a). (a) shows that ε fluctuates and large ε areas locally exist like blue regions. Moreover, (b) under higher Y of 0.25 shows that there are two ε distribution with a lower-ε area on R_2 region and a higher-ε area on R_3 region, where the average ε values of a lower-ε and a high-ε area are 0.25 and 1.7%, respectively. The frequency of a lower-ε area is higher than that of a high-ε area. On the other hand, (c) under lower Y of 0.14 shows only one ε Gaussian-type distribution with the average ε of 0.7%.

is mainly attributable to the smaller $\Delta a/a_S$ of the R_2 area, because of the smaller fabrication area of 3C-SiC in the case of a low Y, as shown by the low G band intensity in Fig. 6(b). Therefore, it is possible to suppress the compressive strain variation by increasing the C ion dose for forming a full 3C-SiC area in the C segregation layer.

The ε of the R_0 layers as a function of Y can be also evaluated by UV-Raman spectroscopy. The compressive ε (%) also causes upshift $\Delta\omega$ (cm^{-1}) of the Raman speak of LO Si–Si vibration in R_0 layers. Namely,[11)]

$$\varepsilon = 0.117\Delta\omega. \tag{4}$$

Figure 9 shows that $\Delta\omega$ (circles) increases with increasing Y, and thus the ε of the R_0 layers calculated using Eq. (4) increases with increasing Y, where $N_L = 5$. The triangles and square show the average ε values of the R_2 and R_3 areas shown in Figs. 8(b) and 8(c). The ε measurement area of the R_0 layers is the Raman laser beam diameter of 1 µm. Thus, the ε value of a large R_2 area is almost equal to the Raman data, but the ε of R_3 with a smaller area is much higher than the Raman data.

3.2 Novel PL properties in 2D-/3D-$Si_{1-Y}C_Y$

Here, we study the E_{EX}, Y, and N_L dependences of PL properties of $Si_{1-Y}C_Y$ layers at room temperature. We also discuss the band structure modulation.

Figure 10 shows the E_{EX} dependence of the PL spectra of 2D $Si_{1-Y}C_Y$, where $Y = 0.25$ and $N_L = 5$. The blue, green, and red lines show the data obtained at $E_{EX} = 3.8$, 2.8, and

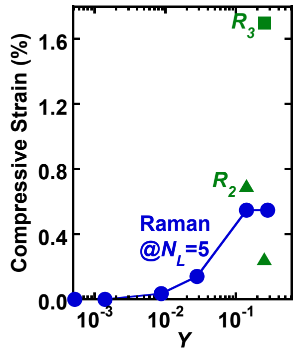

Fig. 9. (Color online) Biaxial ε as a function of Y. Circles shows ε evaluated using Eq. (2) with the peak Si-Raman upshift of 2D $Si_{1-Y}C_Y$, where $E_{EX} = 3.8\,\text{eV}$ and $N_L = 5$. Triangles show the average ε values of a lower-ε area shown in Figs. 8(b) and 8(c), where $N_L = 162$, and the ε values of a lower-ε area is equal to the Raman data. Square shows the average ε of a high-ε area in Fig. 8(b).

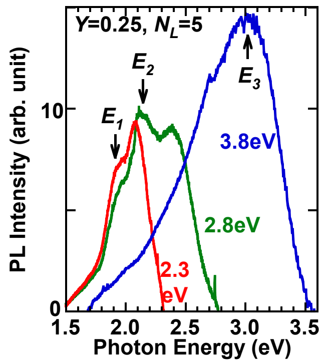

Fig. 10. (Color online) E_{EX} dependence of the PL spectra of 2D $Si_{1-Y}C_Y$, where $Y = 0.25$ and $N_L = 5$. The blue, green, and red lines show the data under $E_{EX} = 3.8$, 2.8, and 2.3 eV, respectively. PL spectra strongly depend on E_{EX}, because PL emission condition should obey the rule of $E_{EX} \geq E_G$. As expected, we confirmed the three PL peaks of I_1, I_2, and I_3 from R_1–R_3 regions shown in Fig. 7, respectively. PL measurement of 2D $Si_{1-Y}C_Y$ with high E_G strongly requires higher E_{EX}. Higher E_3 of ~3 eV (UV PL emission) can be achieved under $E_{EX} = 3.8\,\text{eV}$.

2.3 eV, respectively. PL spectra strongly depend on E_{EX}, because the PL emission conditions should obey the rule that $E_{EX} > E_G$. As expected from Fig. 7, we actually confirmed the presence of three PL peaks of I_1, I_2, and I_3 from the R_1 to R_3 regions with different E_G values, respectively. For the PL measurement of 2D $Si_{1-Y}C_Y$ with high E_G, such as E_3, a higher E_{EX} is strongly required. E_3 of ~3 eV, whose peak wavelength λ_{PL} is approximately 410 nm (UV PL emission), can be achieved at $Y = 0.25$ and $E_{EX} = 3.8\,\text{eV}$. In the case of E_{EX} of 3.8 eV, the I_1 and I_2 peaks are too weak to be observed clearly, compared with a large I_3. In order to observe the I_1 and I_2 peaks clearly, it is required to decrease ($E_{EX} - E_G$).

Next, Fig. 11(a) shows the Y dependence of the PL spectra of 2D $Si_{1-Y}C_Y$, where $E_{EX} = 3.8\,\text{eV}$ and $N_L = 5$. E_1 (1.9 eV), E_2 (2.2 eV), and E_3 (3.0 eV) are attributable to peak E_{PH} (I_{PL}) from the R_1 to R_3 layers in Fig. 7, respectively. Each I_{PL} and E_{PH} drastically increase with increasing Y, which was already demonstrated at $Y \leq 0.13$ in our previous paper.[34)] In particular, I_3 can be clearly observed only at $Y = 0.25$. In addition, Fig. 11(b) shows I_3 vs the Raman intensity I_G of the G band of 3C-SiC layers at various Y values determined using the same data in Figs. 6(b) and 11(a), where $N_L = 5$.

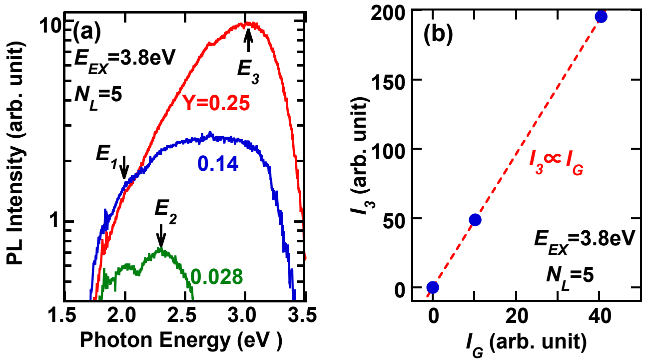

Fig. 11. (Color online) Y dependence of (a) PL spectra of 2D $Si_{1-Y}C_Y$ and (b) I_3 vs I_G (circles) obtained by UV-Raman spectroscopy shown in Fig. 6(b), where $E_{EX} = 3.8$ eV and $N_L = 5$. E_1 (I_1), E_2 (I_2), and E_3 (I_3) are attributable to the peak E_{PH} (I_{PL}) of R_1–R_3 regions (Fig. 7), respectively. Dashed line in (b) with the correlation coefficient of ∼1 shows that I_3 completely correlates with I_G.

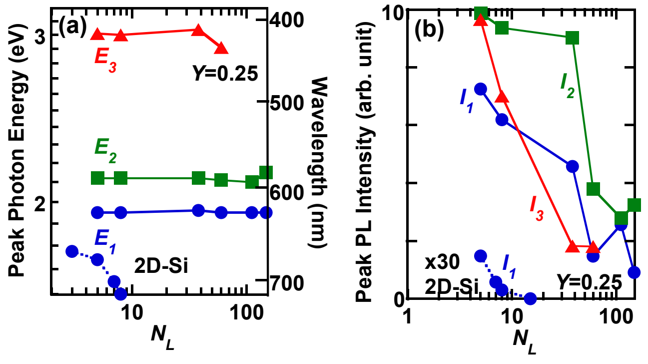

Fig. 13. (Color online) N_L dependence of (a) each E_{PH} and (b) peak I_{PL} of $Si_{1-Y}C_Y$, where $Y = 0.25$. E_{EX} values of E_1 (circles), E_2 (squares), and E_3 (triangles) are 2.3, 2.8, and 3.8 eV, respectively. The right vertical axis in (a) shows the photon wavelength. The dotted lines in (a) and (b) show experimental E_{PH} and 30 times the peak I_1 of the 2D Si, respectively, and both results strongly depend on N_L. However, (a) shows that E_{PH} of $Si_{1-Y}C_Y$ is almost independent of N_L. The I_1 and I_2 of $Si_{1-Y}C_Y$ can be observed even under $162 \geq N_L > 10$, whereas 2D Si can emit PL photons under only $N_L \leq 8$. In addition, I_3 can be observed at $N_L \leq 60$.

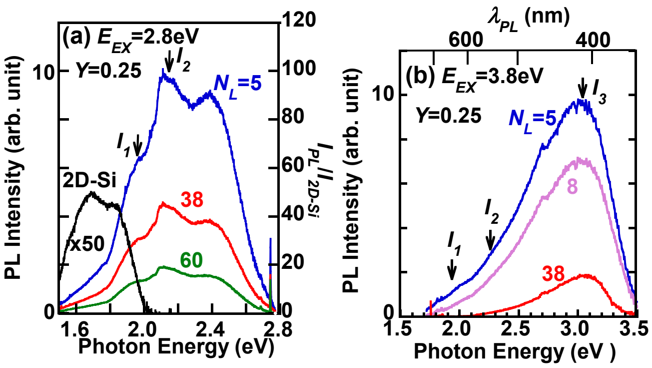

Fig. 12. (Color online) N_L dependence of the PL spectra of $Si_{1-Y}C_Y$ excited by (a) 2.8 and (b) 3.8 eV lasers, where $Y = 0.25$. The black line in (a) shows 50 times the I_{PL} of 2D Si at $N_L = 5$, and the right vertical axis shows the I_{PL} enhancement factors of $Si_{1-Y}C_Y$ normalized by the peak I_{PL} of 2D Si at $N_L = 5$ ($I_{PL\text{-}2D}$), and thus the peak I_{PL} of $Si_{1-Y}C_Y$ at $N_L = 5$ is approximately 100 times as large as that of 2D Si. The upper axis in (b) shows the PL photon wavelength, and the λ_{PL} of $Si_{1-Y}C_Y$ at $N_L = 5$ can be observed at wavelengths longer than 350 nm in the UV region. In both E_{EX} values, even in $N_L \gg 10$, 3D $Si_{1-Y}C_Y$ layers can emit PL photons. Moreover, I_{PL} of $Si_{1-Y}C_Y$ strongly depends on N_L, whereas E_{PH} of $Si_{1-Y}C_Y$ is independent of N_L.

The dashed line with the correlation coefficient of ∼1 shows that I_3 completely correlates with I_G. Thus, I_3 is experimentally verified to be the PL emission from the 3C-SiC area shown in Fig. 7. As a result, 3C-SiC can be formed only in the C segregation area under high-Y condition, and E_3 is considered to be the E_G of the 3C-SiC layer. The high E_3 of approximately 3 eV is possibly attributable to the QCE of 2D electrons confined in 2 nm 3C-SiC layers similarly to the 2D Si layers,[11] because the E_G of bulk 3C-SiC is only 2.2 eV.[33]

Next, we examine the PL properties of $Si_{1-Y}C_Y$ in a wide range of N_L values including the 3D-$Si_{1-Y}C_Y$ layer ($N_L > 10$). Figures 12(a) and 12(b) show the N_L dependence of the PL spectra of $Si_{1-Y}C_Y$ layers excited by 2.8 and 3.8 eV lasers, respectively, where $Y = 0.25$. The black line in Fig. 12(a) shows the I_{PL} enlarged to 50 times the initial I_{PL} of 2D Si at $N_L = 5$, and the right vertical axis shows the I_{PL} enhancement of $Si_{1-Y}C_Y$ normalized by the peak I_{PL} of 2D Si at $N_L = 5$. The upper axis in Fig. 12(b) shows the PL photon wavelength. I_1, I_2, and I_3 all drastically decrease with increasing N_L, but the I_{PL} of $Si_{1-Y}C_Y$ can be observed even at $N_L = 60$, that is, 3D Si–C layers. Moreover, Fig. 12(a) shows that at $N_L = 5$, the peak I_{PL} of $Si_{1-Y}C_Y$ is approximately 100 times larger than that of 2D Si; thus, the PL emission rate drastically increases in the $Si_{1-Y}C_Y$ layer, but the physical mechanisms (such as, the longer life time of generated electrons, or smaller nonradiative time constant of electrons, or the increased absorption coefficient of excited photons)[34] are not understood at present. Thus, the PL emission peak with E_{PH} of approximately 1.7 eV[7] from a 2D-R_0 area with $N_L < 10$ is too weak to be observed in Fig. 12(a). Moreover, the E_{PH} of $Si_{1-Y}C_Y$ in Figs. 12(a) and 12(b) is much higher than that of 2D Si, but it is noted that E_1, E_2, and E_3 are independent of N_L. On the other hand, the E_{PH} of 2D Si strongly depends on N_L, as will be discussed in detail later. Figure 12(b) also shows that the λ_{PL} of $Si_{1-Y}C_Y$ can be observed at wavelength longer than 350 nm of the UV region.

Here, we summarize the N_L dependence of PL properties of $Si_{1-Y}C_Y$ in a wide range of $5 \leq N_L \leq 162$, compared with that of the PL properties of 2D Si with $N_L = 5$. Figures 13(a) and 13(b) show the N_L dependence of each E_{PH} and peak I_{PL}, respectively, where $Y = 0.25$. E_{EX} values for E_1 (circles), E_2 (squares), and E_3 (triangles) are 2.3, 2.8, and 3.8 eV, respectively. The right vertical axis in Fig. 13(a) shows the photon wavelength. The dotted lines in Figs. 13(a) and 13(b) show experimental the E_{PH} and the I_{PL} enlarged to 30 times the peak I_{PL} of 2D Si, respectively. The I_1 and I_2 of $Si_{1-Y}C_Y$ can be observed even at $162 \geq N_L > 10$, whereas 2D Si can emit PL photons only at $N_L \leq 8$. Moreover, the I_3 of the 3C-SiC layer near the BOX interface cannot be observed at $N_L > 60$, as shown in Fig. 14. Figure 13(a) shows that the E_{PH} of $Si_{1-Y}C_Y$ is almost independent of N_L even under $162 \geq N_L$. On the other hand, the E_{PH} of 2D Si strongly depends on N_L, since the band structure modulation of 2D Si is attributable to QCEs of electrons in a finite Si thickness.[11] Therefore, there are three distinguishing PL properties of Si–C layers, that is, 1) higher E_{PH}, 2) very strong I_{PL}, and 3) N_L independence of E_{PH}. Thus, the physical mechanism of the PL emission of 2D-/3D-$Si_{1-Y}C_Y$ is much different from

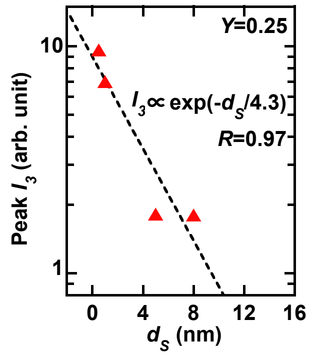

Fig. 14. (Color online) d_S dependence of peak I_3 (triangles) of 2D/3D-$Si_{1-Y}C_Y$, where $E_{EX} = 3.8$ eV and $Y = 0.25$. Experimental data almost obeys Eq. (5) (dashed lines) with fitting $\lambda_0 \approx 4.3$ nm, where the correlation coefficient is 0.97.

that of 2D Si. In the oxidation process of the thinning of SOI, the thicknesses of R_1 to R_3 areas are kept almost constant to be approximately 2 nm, as shown in Figs. 3 and 5, because as discussed above, the surface oxidation does not affect the BOX interface.[34] Thus, only the thickness of the R_0 area decreases with increasing oxidation time. Consequently, as shown in Fig. 7 discussion, the measured PL emission of $Si_{1-Y}C_Y$ mainly originates from the local area from R_1 to R_3 near the BOX interface. In addition, a thicker R_0 area with $N_L > 10$ cannot emit PL photons, as discussed for 2D Si [Fig. 13(a)]. Thus, the decrease in I_{PL} with increasing N_L in Fig. 13(b) is caused by the power reduction of the incident excitation laser beam in the buried C segregation layer near the BOX interface, as shown in Fig. 14.

Here, we introduce a model for the strong N_L dependence of I_3 intensity of the R_3 area of the 3C-SiC layer near the BOX interface, as shown in Fig. 13(b). The 3C-SiC layer is buried near the BOX interface at the depth d_S from the Si surface. The excitation laser flux $I_{EX}(x)$ at the depth x from the Si surface can be expressed by $I_{EX}(x) = I_0 \exp(-x/\lambda_{EX})$, where I_0 is the laser flux at the Si surface and λ_{EX} is the penetration length of laser photons in the Si layer. As a result, the PL intensity $I_{PL}(x)$ of the buried region at the depth x from the surface can be obtained using the following equation, assuming that the PL emission rate is η.

$$\begin{aligned} I_{PL}(x) &= \eta I_{EX}(x) \exp\left(-\frac{x}{\lambda_{PL}}\right) \\ &= \eta I_0 \exp[-(\lambda_{EX}^{-1} + \lambda_{PL}^{-1})x] = \eta I_0 \exp\left(-\frac{x}{\lambda_0}\right), \end{aligned} \quad (5)$$

where λ_{PL} is the penetration length of PL emission photons in the Si layer, and the effective penetration length λ_0 is obtained using $\lambda_0^{-1} \equiv \lambda_{EX}^{-1} + \lambda_{PL}^{-1}$. λ_{EX} at 3.8 eV and λ_{PL} at 3 eV in the bulk-Si layer are 8.7 and 92 nm,[26] respectively; thus, the calculated λ_0 is approximately 7.9 nm.

Figure 14 shows the d_S dependence of peak I_3 (triangles), where $Y = 0.25$. Experimental I_3 data can be well fitted using Eq. (5), where the correlation coefficient is 0.97. λ_0 is experimentally fitted to be 4.3 nm, which is approximately 2 times as large as the calculated λ_0 of 7.9 nm. The small λ_0 in Fig. 14 is considered to be attributable to the reduced penetration length effects (or enhanced absorption coefficient) in $Si_{1-Y}C_Y$ layers, similar to the enhanced absorption coefficient in the 2D Si layer.[39] As a result, I_3 photons cannot be emitted at $N_L > 60$, since the excitation laser photons cannot reach to the buried R_3 area under the thick R_0 area of $d_S > 10$ nm. Thus, we also verified from Fig. 14 that I_3 photons are emitted from the buried R_3 area at the depth d_S from the Si surface.

3.3 Si–C technique application in devices

Here, we firstly discuss the Si–C technique application in 2D-CMOS devices. Using the local hot-C^+-ion implantation technique by a mask process, E_G engineering in the local area of 2D Si layers can be easily realized. The R_3 region of 3C-SiC is the buried layer near the BOX interface, and in addition, the electron affinity χ of bulk 3C-SiC is 4 eV,[40] which is almost the same as that χ of 3D-Si (4.05 eV).[26] As a result, the heterojunction between the source-3C-SiC and channel-2D Si has no band offset at the conduction band for high-speed n-SHOT,[28] although the valence band offset is suitable for p-SHOT. On the other hand, the compressively strained R_0 region shown in Fig. 8 is considered to have large E_G, because of the compressive-strain-induced E_G expansion.[11] Thus, the R_0 region can be a candidate for the source region of the n-SHOT with the 2D Si channel. For example, the conduction band offset ΔE_C between the R_0 source and the 2D Si channel is equal to $(E_1 - E_{2D})/2$, as shown in Fig. 13(b), where E_{2D} is E_G of 2D Si. As a result, at the ballistic transport limit, the electron injection velocity from the source into the channel can reach $(2\Delta E_C/m^*)^{1/2}$, where m^* is effective electron mass in the 2D Si channel.[28] On the other hand, the stacking faults of 3C-SiC [Fig. 5(b)] beneath the R_0 region exist inside the source diffusion layer, and thus do not affect the SHOT performance.

On the other hand, the high I_{PL} of Si–C layers in the regions form R_1 to R_3 with the maximum enhancement factor of approximately 100, compared with the I_{PL} of 2D Si shown in Fig. 12(a), is very promising for Si photonic devices in the UV/visible region. In particular, the advantageous property is the PL emission even from 3D 22 nm Si–C layers which is not necessary to form the nano structures by difficult and complicated processes. Moreover, the second merit is that the peak λ_{PL} from the NIR to UV regions can be easily controlled by adjusting Y.[34]

4. Conclusions

We successfully fabricated 2D/3D-$Si_{1-Y}C_Y$ layers by the simple process of the combination of hot-C^+-ion implantation at the substrate temperature of 900 °C and the oxidation process, where $5 \times 10^{12} \leq D_C \leq 4 \times 10^{16}\,cm^{-2}$. We experimentally studied the material structures and PL properties of 2D-/3D-$Si_{1-Y}C_Y$ layers at $Y \leq 0.25$ and $5 \leq N_L \geq 162$. The C 1s spectrum obtained by XPS shows that C atoms segregate at the BOX interface, which is the characteristic feature of the hot-ion implantation process. The maximum Y in this study was 0.25 under $D_C = 4 \times 10^{16}\,cm^{-2}$. HRTEM and HAADF-STEM analyses of the 22 nm $Si_{0.75}C_{0.25}$ layer show that 3C-SiC layers are partially formed in the C segregation area near the BOX interface. As a result, $Si_{1-Y}C_Y$ layers in the C segregation layers are mainly divided into three regions of partial 3C-SiC (R_3 region), high-C Si–C alloy (R_2 region), and Si–C alloy (R_1 region) in the slope low-C area. On the other hand, the Si layer (R_0 region) on the C segregation layer with a smaller lattice constant is compressively strained.

Band structures are analyzed by the PL method at room temperature excited at E_{EX} from 2.3 to 3.8 eV. As expected, we confirmed three PL peaks I_1–I_3 from the three local regions of R_1, R_2, and R_3 area near the BOX interface even in 3D Si–C layers at $N_L \leq 162$, although 2D Si shows PL emission only at $N_L < 10$. PL spectra in the UV and visible regions strongly depend on E_{EX} and Y. However, the E_{PH} of 2D-/3D Si–C layers are independent of N_L, whereas the I_{PL} and E_{PH} of 2D Si rapidly increase with decreasing N_L, because of QCE of 2D electrons in a finite Si. Under $Y = 0.25$, a higher E_{PH} of 3 eV and a UV PL emission (>350 nm) from 3C-SiC layers can be realized. In addition, the I_{PL} and E_{PH} of Si–C layers rapidly increase with increasing Y, resulting in the I_{PL} enhancement factor of approximately 100 compared with the I_{PL} of 2D Si. Consequently, Si–C technique by the hot-C^+-ion implantation method is very promising for both local E_G engineering for CMOS-SHOT and Si-based photonic devices from the NIR region to the UV region.

1) J.-P. Colinge, *Silicon-on-Insulator Technology* (Kluwer, Dordrecht, 2004).
2) T. Irisawa, T. Numata, T. Tezuka, K. Usuda, S. Sugiyama, and S. Takagi, IEEE Trans. Electron Devices **55**, 649 (2008).
3) S. Saito, D. Hisamoto, H. Shimizu, H. Hamamura, R. Tsuchiya, Y. Matsui, T. Mine, T. Arai, N. Sugii, K. Torii, S. Kimura, and T. Onai, Jpn. J. Appl. Phys. **45**, L679 (2006).
4) S. Saito, N. Sakuma, Y. Suwa, H. Arimoto, D. Hisamoto, H. Uchiyama, J. Yamamoto, T. Sakamizu, T. Mine, S. Kimura, T. Sugawara, M. Aoki, and T. Onai, IEDM Tech. Dig., 2008, 19.5.
5) L. Pavesi and D. J. Lockwood, *Silicon Photonics* (Springer, Berlin, 2004).
6) T. Mizuno, K. Tobe, Y. Maruyama, and T. Sameshima, Jpn. J. Appl. Phys. **51**, 02BC03 (2012).
7) T. Mizuno, T. Aoki, Y. Nagata, Y. Nakahara, and T. Sameshima, Jpn. J. Appl. Phys. **52**, 04CC13 (2013).
8) T. Mizuno, Y. Nakahara, Y. Nagata, Y. Suzuki, T. Aoki, and T. Sameshima, Jpn. J. Appl. Phys. **53**, 04EC08 (2014).
9) T. Mizuno, Y. Nagata, Y. Suzuki, Y. Nakahara, T. Aoki, and T. Sameshima, Jpn. J. Appl. Phys. **53**, 04EC09 (2014).
10) T. Mizuno, Y. Nagamine, Y. Suzuki, Y. Nakahara, Y. Nagata, T. Aoki, and T. Sameshima, Jpn. J. Appl. Phys. **54**, 04DC05 (2015).
11) T. Mizuno, Y. Suzuki, Y. Nagamine, Y. Nakahara, Y. Nagata, T. Aoki, and T. Maeda, Jpn. J. Appl. Phys. **54**, 04DC02 (2015).
12) N. Fukata, T. Oshima, K. Murakami, T. Kizuka, T. Tsurui, and S. Ito, J. Appl. Phys. **100**, 024311 (2006).
13) K. W. Adu, H. R. Gutierrez, and P. C. Eklund, in *Nanosilicon*, ed. V. Kumar (Elsevier, Amsterdam, 2008) Chap. 7.
14) H. Richter, Z. P. Wang, and L. Ley, Solid State Commun. **39**, 625 (1981).
15) I. H. Campbell and P. M. Fauchet, Solid State Commun. **58**, 739 (1986).
16) L. Donetti, F. Gámiz, J. B. Roldán, and A. Godoy, J. Appl. Phys. **100**, 013701 (2006).
17) K. Uchida, H. Watanabe, A. Kinoshita, J. Koga, T. Numata, and S. Takagi, IEDM Tech. Dig., 2002, p. 47.
18) K. Uchida, J. Koga, and S. Takagi, J. Appl. Phys. **102**, 074510 (2007).
19) G. Tsutsui, M. Saitoh, and T. Hiramoto, IEEE Trans. Electron Devices **26**, 836 (2005).
20) B. K. Agrawal and S. Agrawal, Appl. Phys. Lett. **77**, 3039 (2000).
21) M. Tabe, M. Kumezawa, and Y. Ishikawa, Jpn. J. Appl. Phys. **40**, L131 (2001).
22) Z. H. Lu and D. Grozea, Appl. Phys. Lett. **80**, 255 (2002).
23) S. S. Iyer and Y.-H. Xie, Science **260**, 40 (1993).
24) Y. Takahashi, T. Furuta, Y. Ono, T. Ishiyama, and M. Tabe, Jpn. J. Appl. Phys. **34**, 950 (1995).
25) H. Omi, T. Kawamura, S. Fujikawa, Y. Tsusaka, Y. Kagoshima, and J. Matsui, Appl. Phys. Lett. **86**, 263112 (2005).
26) S. M. Sze and K. K. Ng, *Physics of Semiconductor Devices* (Wiley, New York, 2007).
27) T. Mizuno, N. Sugiyama, T. Tezuka, Y. Moriyama, S. Nakaharai, T. Maeda, and S. Takagi, IEEE Trans. Electron Devices **52**, 2690 (2005).
28) T. Mizuno, Y. Moriyama, T. Tezuka, N. Sugiyama, and S. Takagi, Jpn. J. Appl. Phys. **50**, 010107 (2011).
29) K.-J. Chui, K.-W. Ang, N. Balasubramanian, M.-F. Li, G. S. Samudra, and Y.-C. Yeo, IEEE Trans. Electron Devices **54**, 249 (2007).
30) L. R. Tessler and I. Solomon, Phys. Rev. B **52**, 10962 (1995).
31) W. Liu, M. Zhang, C. Lin, Z. Zeng, L. Wang, and P. K. Chu, Appl. Phys. Lett. **78**, 37 (2001).
32) S. T. Pantelides and S. Zollner, *Silicon-Germanium Carbon Alloys* (Taylor & Francis, New York, 2002).
33) J. Fan and P. K. Chu, *Silicon Carbide Nanostructure* (Springer, Cham, 2014).
34) T. Mizuno, Y. Nagamine, Y. Omata, Y. Suzuki, W. Urayama, T. Aoki, and T. Sameshima, Jpn. J. Appl. Phys. **55**, 04EB02 (2016).
35) T. Mizuno, Y. Nagamine, U. Omata, M. Yokoyama, T. Aoki, and T. Sameshima, Ext. Abstr. Solid State Devices and Materials, 2016, p. 633.
36) Web [http://www.soitec.com/en/].
37) Y. Hijikata, H. Yaguchi, and S. Yoshida, Appl. Phys. Express **2**, 021203 (2009).
38) D. N. Talwar and Z. C. Feng, Comput. Mater. Sci. **30**, 419 (2004).
39) T. Mizuno, Y. Nagata, Y. Suzuki, Y. Nakahara, T. Tanaka, T. Aoki, and T. Sameshima, Ext. Abstr. Solid State Devices and Materials, 2013, p. 96.
40) S. Yu. Davydov, Semiconductors **41**, 696 (2007).